NANO LETTERS

Letter

pubs.acs.org/NanoLett

Atomically Thin Graphene Windows That Enable High Contrast Electron Microscopy without a Specimen Vacuum Chamber

Yimo Han,[†] Kayla X. Nguyen,[‡] Yui Ogawa,[‡,∥] Jiwoong Park,[*,‡,§] and David A. Muller[*,†,§]

[†]Department of Applied and Engineering Physics, Cornell University, Ithaca, New York 14853, United States

[‡]Department of Chemistry and Chemical Biology, Cornell University, Ithaca, New York 14853, United States

[§]Kavli Institute at Cornell for Nanoscale Science, Ithaca, New York 14853, United States

[∥]Institute for Materials Chemistry and Engineering, Kyushu University, Kasuga, Fukuoka 816-8580, Japan

Supporting Information

ABSTRACT: Scanning electron microscopes (SEMs) require a high vacuum environment to generate and shape an electron beam for imaging; however, the vacuum conditions greatly limit the nature of specimens that can be examined. From a purely scattering physics perspective, it is not necessary to place the specimen inside the vacuum chamber—the mean free paths (MFPs) for electron scattering in air at typical SEM beam voltages are 50−100 μm. This is the idea behind the airSEM, which removes the specimen vacuum chamber from the SEM and places the sample in air. The thickness of the gas layer is less than a MFP from an electron-transparent window to preserve the shape and resolution of the incident beam, resulting in comparable imaging quality to an all-vacuum SEM. Present silicon nitride windows scatter far more strongly than the air gap and are currently the contrast and resolution limiting factor in the airSEM. Graphene windows have been used previously to wrap or seal samples in vacuum for imaging. Here we demonstrate the use of a robust bilayer graphene window for sealing the electron optics from the room environment, providing an electron transparent window with only a 2% drop in contrast. There is a 5-fold-increase in signal/noise ratio for imaging compared to multi-MFP-thick silicon nitride windows, enabling high contrast in backscattered, transmission, and surface imaging modes for the new airSEM geometry.

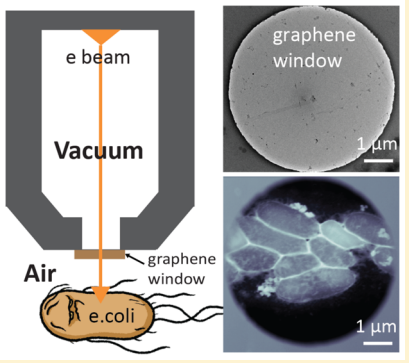

KEYWORDS: *SEM, AirSEM, STEM, graphene, electron scattering*

Scanning electron microscopy (SEM) is a ubiquitous tool in science and engineering applications, used to observe nanometer and micron-sized structures. In general, vacuum SEM (VSEM), or conventional SEM, requires specimens that are stable in vacuum and electrically conductive. However, many chemical and biological specimens are only stable in a gas or liquid environment and are electrically insulating, which makes their direct imaging by VSEM challenging. One approach for imaging such samples is to remove them from their native environments and pretreat them before imaging in vacuum using staining, fixing, and coating with thin conductive layers, which often changes the morphology or compositions of the specimens. To avoid this problem, multiple electron microscopy techniques suitable for gaseous or liquid environments have been developed. For example, environmental SEM (ESEM)[1] is able to image specimens at partial atmospheric pressures using differential pumping and a pressure-limiting aperture but gives much lower contrast and resolution than a VSEM, as the gas path length (GPL) in an ESEM is 2−5 times longer than the electron mean free path (MFP). More recently, atmospheric SEM[2] was developed, which employs an inverted electron optical column and uses a SiN_x window to separate the specimen that is placed on top of the window from the electron optics in vacuum.

In the airSEM design,[3−5] which is schematically shown in Figure 1a, an upright SEM geometry rather than the inverted geometry of atmospheric SEM is used instead. As in a previous SEM designs, the electron gun and optics are maintained in vacuum, but an electron-transparent window, backed by an additional ion pump, is placed below the objective lens to seal the column. The column is based on a Mira Tescan 3 with a Schottky field emission gun, and a gun vacuum of 7×10^{-10} Torr. A separate ion pump and gun valve are used to provide a degree of differential pumping down the column and protect the gun when windows break or need to be changed. Because the sample is not in direct contact with the window, the window can be much thinner (~10−20 nm SiN_x) and does not need to be replaced as often (typically every few weeks). Without the need to pump down a specimen chamber or change the imaging window, sample transfer and loading times are negligible. Moreover, as with other environmental SEM

Received: July 20, 2016
Revised: November 10, 2016
Published: November 14, 2016

DOI: 10.1021/acs.nanolett.6b03016
Nano Lett. 2016, 16, 7427−7432

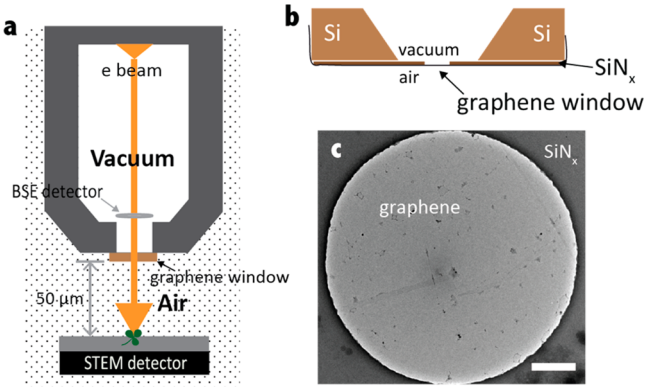

Figure 1. Graphene window configuration in airSEM. (a) Schematic of airSEM, which has the same gun and column as the Tescan Mira3. The specimens are placed directly out in air and separated by a thin graphene window from the electron optics that are in a vacuum of 10^{-6} Torr and the Schottky field emission gun at 7×10^{-10} Torr. The atomically thin graphene window, together with 50 μm gas path length (GPL), is transparent to fast electrons. (b) Schematic of a cross section of the graphene window fabricated by transferring graphene to a holey SiN_x window, which can be easily mounted to the airSEM. (c) TEM image of a fabricated bilayer graphene window shown as the bright central disk. As the airSEM beam is not focused on the window, small nonuniformities have little impact on the imaging. The scale bar is 1 μm.

methods, the surface charges are compensated by the ions from the air, making it possible to image insulating specimens without a conductive coating. As a result, airSEM enables high throughput imaging of specimens in air. However, the use of SiN_x windows is still the performance-limiting factor in airSEM although they are only tens of nanometers thick. Because of its higher atomic numbers and densities, the window causes more electron scattering events than does the air.[6] In order to realize the optimal performance of airSEM, the electron scattering by the window needs to be minimized, which can be achieved by decreasing its thickness and using a window material with a lower atomic number.

Graphene is an ideal candidate material for electron transparent windows in airSEM; it is composed of only one- or two-atom-thick monolayer of carbon, a lighter element than silicon nitride, and can be used to separate vacuum (10^{-6} Torr for the airSEM column) from 1 atm of pressure for a long period of time due to its intrinsically high mechanical strength, impermeability, and ability to effectively seal attaching interfaces.[7−9] While graphene has been previously used as an electron-transparent film to directly wrap various specimens in gaseous and liquid environments for transmission electron microscopy (TEM),[10,11] VSEM,[12,13] and photoelectron spectroscopy,[14] its use as a free-standing atmospheric and electron transparent window that eliminates the specimen vacuum chamber has not been reported. Here, we demonstrate the realization and use of free-standing and reusable bilayer graphene windows for airSEM, enabling electron imaging without a specimen vacuum chamber, and yet still retaining high contrast and resolution for a variety of SEM imaging modes.

Figure 1b and c first shows a cross-sectional schematic and a representative TEM image of the bilayer graphene window we developed (bright center in Figure 1c; diameter: 5 μm). Our graphene windows were fabricated by transferring monolayer graphene films, grown by chemical vapor deposition,[15,16] twice onto a SiN_x frame (dark region) (see Supporting Information for detailed fabrication process). We note that bilayer graphene was used instead of monolayer graphene as it dramatically increases the fabrication yield while reducing leakage or tearing during operation of the airSEM. As discussed in the Supporting Information, the most likely failure mode of the window was radiation damage of residual contamination left over from the window manufacture, and initially clean windows could survive for many weeks to months.

We expect our bilayer graphene windows to be highly electron transparent compared with SiN_x windows. Figure 2a

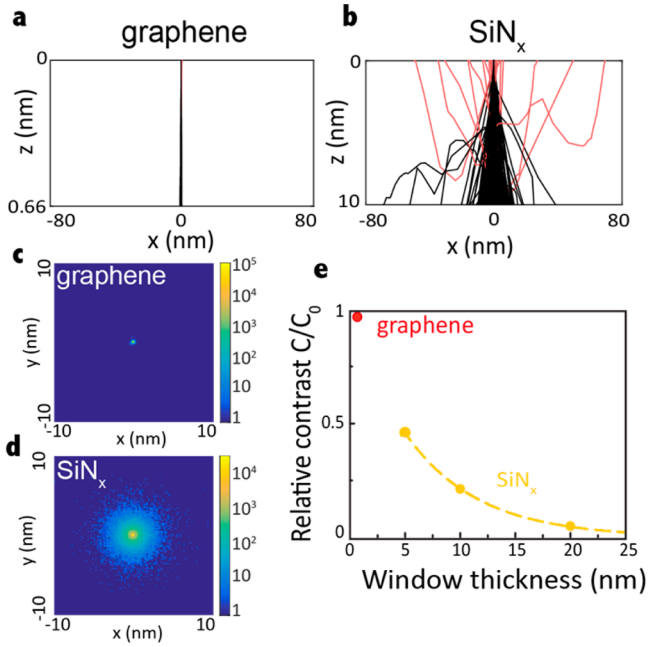

Figure 2. Monte Carlo simulation of electron scattering. (a, b) Comparison of electron paths in a bilayer graphene window (0.66 nm) and a SiN_x window (10 nm). The black and red paths respectively indicate electrons transmitted through the window and electrons backscattered by the window (0.01% for graphene window and 0.4% for SiN_x window). (c, d) Electron intensity color map at the window-air interface shows less scattering in the graphene window contributing to a greatly reduced halo and thus higher contrast. (e) Transmission image contrast from a gold nanoparticle on amorphous carbon support using a graphene window and SiN_x windows of different thicknesses for a 50 μm gas path length in air. The contrast was normalized to the no-window contrast C_0. The dashed yellow line is the fitting curve. All simulations were done with 7 kV electron energy.

and b show Monte Carlo simulations of electron paths (7 kV acceleration voltage) through a graphene window and a SiN_x window (10 nm thick), respectively. While about three-quarters of the electrons are scattered out of the incident beam to different angles in the SiN_x window, 97% of electrons pass directly through the graphene window without scattering. As a result, the electron beam retains more of its initial, focused shape when scattered through graphene windows, contributing to higher contrast and therefore dose-limited spatial resolution, as depicted in Figure 2c and d where the electron intensity at the window−air interface is mapped. Figure 2e shows the simulated image contrast for a graphene window and SiN_x windows of varying thickness, where the contrast (as we defined in eq 1) was normalized to the no-window contrast C_0, where the electrons scatter in air only. We observed that

DOI: 10.1021/acs.nanolett.6b03016
Nano Lett. 2016, 16, 7427−7432

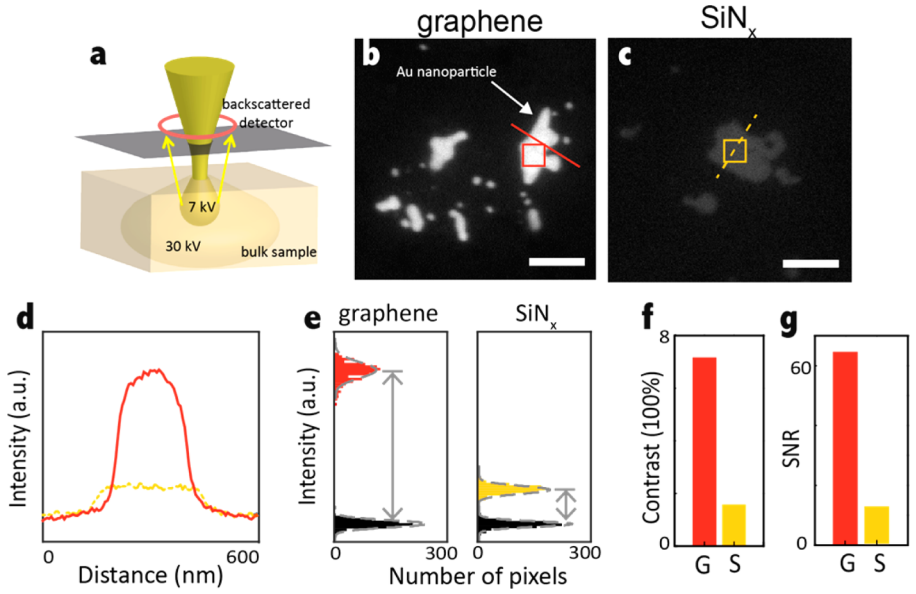

Figure 3. Comparison of graphene and SiN_x windows in backscattered electron (BSE) mode. (a) Schematic of airSEM BSE mode, which has better resolution with lower electron beam energies. Here we used 7 kV. (b, c) Experimental airSEM BSE images of gold nanoparticles on a carbon block, using graphene and SiN_x windows. The scale bars are 500 nm. (d) BSE intensity profiles of gold nanoparticles with graphene (red solid) and SiN_x (yellow dashed) windows extracted from the lines indicated in b and c. (e) Intensity histogram from b and c with the signal peaks (red for graphene and yellow for SiN_x) from Au nanoparticles (squares in b, c) and the background peaks (black for both graphene and SiN_x) from carbon block. The number of pixels are the same for the graphene and SiN_x signals and the background. The gray dashed lines are Gaussian fitting curves. (f and g) Comparisons of measured Weber contrast and SNR for graphene (G) versus SiN_x windows (S).

graphene windows double the image contrast of the thinnest commercially available SiN_x windows (5 nm). Furthermore, the relative contrast with a graphene window is calculated to be 0.98 of the window-free case, consistent with the negligible electron scattering in graphene windows. This suggests that the single scattering regime can be reached in airSEM with graphene windows, resulting in image qualities comparable to those of VSEM.

Altogether, the combination of unique properties of graphene windows, including the high electron transmission, low electron scattering, and high electrical conductivity, significantly improves the imaging performance of airSEM in several imaging modes. Here, we apply them to airSEM in three different imaging modes: backscattered electron (BSE), secondary ion (SI), and scanning transmission electron microscopy (STEM) imaging modes, and discuss the results below.

In Figure 3, we first discuss the BSE mode, one of the most commonly used SEM imaging modes. Figure 3a shows a schematic of BSE mode in airSEM, where electrons are scattered from the sample and travel back up through the window to hit a BSE detector. The spatial resolution of the BSE mode is dominated by the beam spread and depth penetration, both of which grow with the electron beam energy E, scaling roughly as $E^{1.67}$; i.e., the resolution is better (and the signal is more surface specific) with lower E (see Figure 3a). In airSEM, however, higher E (typically 20 kV) is generally used with conventional windows as lower E significantly decreases the electron MFP in the window and gas, and the resultant window multiple scattering leads to poor signal and contrast. As a result, there is a significant trade-off between the resolution and contrast, a limitation that can be overcome by using graphene windows. Monte Carlo simulation shows that graphene windows are highly transparent for all beam energies (1−30 kV) and do not degrade the resolution or contrast. Instead, the gas path length becomes the resolution-limiting factor, and a progressively thinner gas layer is required to retain the contrast and resolution as the beam energy is decreased. (See Supporting Information for optimal beam energies.) Taking this into account, we used a 7 kV electron beam energy in our experiments with graphene windows to allow for a roughly 50 μm window−sample separation. For a 2 kV beam energy, the separation would need to be reduced to under 10 μm, increasing the risk of puncture by a dust particle.

Figure 3b and c shows two airSEM BSE images of gold nanoparticles on amorphous carbon taken using graphene and SiN_x windows, respectively. Here, the display intensity is normalized to the same level of background noise (see the histogram shown in Figure 3e). The intensity profiles measured across nanoparticles of similar sizes (Figure 3d) and the intensity histogram (Figure 3e) generated from Figure 3b and c both show large contrast improvements with graphene windows. For a quantitative comparison, we extracted contrasts and signal-to-noise ratios (SNRs) from Figure 3b and c. We used the Weber definition of contrast:

$$\text{contrast} = \frac{I_s - I_b}{I_b} \times 100\% \quad (1)$$

where I_s is the mean signal extracted from the Gaussian fit (dashed lines) to the signal peaks in the intensity histogram in Figure 3e; similarly, I_b is the mean background value. The measured contrast from the image with the graphene window is 7.17 × 100%, 4.6 times higher than that with SiN_x window (1.56 × 100%, as shown in Figure 3f. SNRs were calculated using the equation:

$$\text{SNR} = \frac{I_s - I_b}{\sigma} \quad (2)$$

DOI: 10.1021/acs.nanolett.6b03016
Nano Lett. 2016, 16, 7427−7432

where σ is the standard deviation of the background peak. The graphene window provided a SNR of 64.7, while the SiN_x window showed a SNR of 12.5 (Figure 3g), a more than 5-fold improvement.

Figure 4 describes another imaging mode for airSEM, the surface imaging (SI) mode, for which graphene windows also provide a significant performance improvement. In airSEM, it is impossible to install a conventional SE detector due to the short range of SEs in air. Instead, ionized molecules are generated by SEs, and those molecules can be collected on the window with a biased specimen stage, as illustrated in Figure 4. To efficiently collect the SI current, the window membrane thus needs to be a good electrical conductor. Here, graphene provides an ideal window material thanks to its high electron transmission and high electrical conductivity. The SI mode, which measures the electrical current carried by secondary ions that are generated from the secondary electrons (SEs), is an analogue to the SE mode in a VSEM that directly measures the collected SEs. Both modes rely on the generation of SEs near the specimen surface, provide much more surface specific information, and are less limited by the size of interaction volumes. Figure 4a demonstrates the surface sensitivity and improved resolution of SI mode by comparing the simultaneous BSE and SI images of a monolayer graphene on the Cu foil. The good contrast from a monolayer of graphene on a thick copper foil for SI imaging but no contrast for BSE imaging provides strong evidence that the SE signal from the primary beam dominates, rather than the SE signal that is produced by the backscattered electrons as they leave the sample.

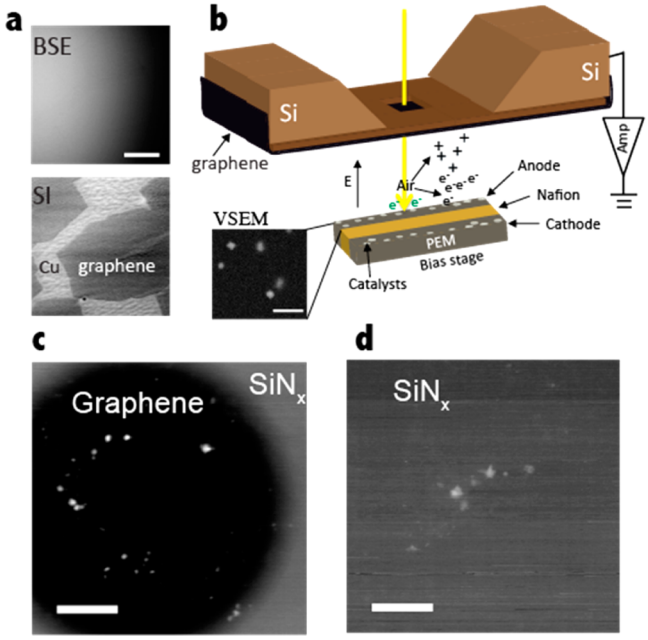

Figure 4. Comparison of graphene and SiN_x windows in surface-imaging (SI) mode. (a) Simultaneous BSE and SI images of a graphene monolayer on the Cu foil. Scale bar: 10 μm. (b) Schematic of imaging a membrane electrode assembly from a proton-exchange-membrane fuel cell cross-section with an SI detector. Ion currents from the drift of ionized air molecules (+ and black e^-) by SEs (green e^-) along the direction of electric field (E) from the biased stage are collected by the window. Inset: vacuum SEM SE image. The scale bar is 400 nm. (c, d) Experimental data of airSEM SI images with graphene and SiN_x windows, respectively. We can also see the SiN_x frame in panel b. The scale bars are 1 μm. Here we used a 15 kV beam energy.

To demonstrate the performance of graphene windows for SI mode in airSEM, we used a cross-section of a membrane electrode assembly (MEA) from a proton exchange membrane fuel cell (PEMFC), where Pt nanoparticles are embedded as catalysts in the PEMFC electrodes (Figure 4b). For comparison, the inset of Figure 4b displays a SE image of the Pt nanoparticles in the MEA, taken using a VSEM. Figure 4c shows a SI image of a similar region taken by airSEM with a graphene window (inside the circular region); it displays excellent spatial resolution and contrast only within the circular graphene window region. However, outside this region, or on a SiN_x membrane with no graphene (Figure 4d), there is poor contrast due to the presence of the less electron transparent SiN_x. The noise streaks along the scan direction in Figure 4d may come from charging of the SiN_x window. These images demonstrate that graphene windows can enable the SI imaging mode of airSEM to reach an image quality comparable to that of SE imaging in VSEM.

Another method for reducing the interaction volume, hence improving the resolution, is STEM imaging which requires a thin specimen. In general, a bright field (BF) or dark field (DF) STEM detector can be used for high-resolution imaging with thin specimens.[4,17] For the airSEM, we built BF and DF detectors using photodiodes that collect transmitted electrons. While a BF STEM detector collects all transmitted electrons, DF detectors have patterned Pt disks with different radii to block the center beam, collecting the electrons scattered by the specimen to high angles only (see Supporting Information for detector geometry). In the thin specimen limit, the resolution of STEM mode is limited by the electron probe size, which is determined by the properties of the electron gun and electron optics. Therefore, we use a higher electron beam energy (20 kV) to minimize probe spreading through the specimen.

The BF-STEM images taken using graphene and SiN_x windows are shown in Figure 5a and b. Here, we used Pt nanoparticles deposited on thin amorphous carbon support as a test specimen. Unlike the BSE and SI images, where the metal particles appeared bright, Pt particles correspond to dark regions (low transmission) in BF-STEM images. Using the same method as in Figure 3e, we plot the transmission intensity histogram in Figure 5c based on the data from Figure 5a and b. They again indicate an improved contrast with a graphene window. Similar behaviors are seen in Figure 5d and e, which show DF-STEM images of the Pt nanoparticles imaged using graphene and SiN_x windows. Our data confirm that using graphene windows improves the contrast for both BF and DF STEM mode in airSEM. As an illustrative example, we also used the DF-STEM mode with graphene windows to image *E. coli* bacteria showing details of the cell membranes (Figure 5f). For biological samples, graphene windows allow high contrast imaging; therefore, they can efficiently reduce the electron dose on the sample, which is a crucial factor for imaging biological objects with electron beams.

To further evaluate the resolution for different modes in airSEM with graphene and SiN_x windows, we used a Fourier-based method[18] (see Supporting Information) to measure the information limit, which is a useful metric for a noise-limited resolution. Table 1 shows that, for all modes, graphene windows offer a more than 2-fold improvement over SiN_x

DOI: 10.1021/acs.nanolett.6b03016
Nano Lett. 2016, 16, 7427−7432

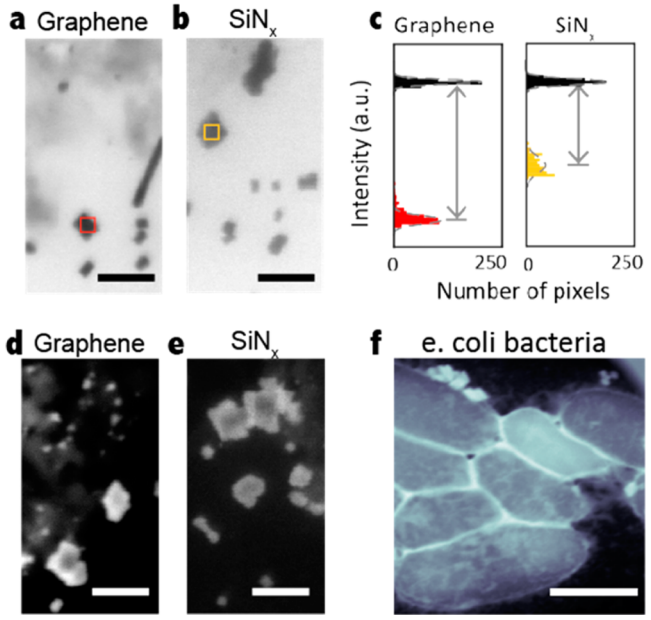

Figure 5. Comparison of graphene and SiN_x windows in scanning transmission electron microscopy (STEM) mode. (a, b) BF-STEM images of Pt nanoparticles on carbon film with graphene and SiN_x windows. The scale bars are 200 nm. (c) Intensity histogram from (a, b) with the signal peaks (red for graphene and yellow for SiN_x) from nanoparticles (squares in a, b) and the background peaks (black for both graphene and SiN_x) from carbon film. The number of pixels is the same for the graphene signal and SiN_x signal and the background. The gray dashed lines are Gaussian fitting curves. (d, e) DF-STEM images with graphene windows and SiN_x windows, respectively. The scale bars are 200 nm. (f) The DF-STEM image of uranium-stained *E. coli* bacteria. The scale bar is 1 μm.

windows. The DF-STEM image with graphene window represents a 2.9 nm information limit.

Table 1. Information Limits for Different Imaging Modes with Graphene and SiN_x Windows

	graphene (nm)	SiN_x (nm)
BSE	14.8	30.3
SI	7.8	20.1
BF-STEM	4.0	11.4
DF-STEM	2.9	5.7

In conclusion, we fabricated bilayer graphene windows, which significantly improved the image contrast and resolution for several imaging modes of airSEM, including BSE, SI, and STEM modes. In addition, the low electron scattering in graphene windows enabled the airSEM to operate at low voltages (7 kV or lower) in the BSE mode, a difficult regime for a SiN_x window. The high electrical conductivity of graphene windows allowed the airSEM to take high-resolution SI images with the image quality comparable to that of SE mode in VSEM. Altogether, our results show that using graphene windows significantly enhances the airSEM's performance, thus enabling a wide range of future applications such as observing untreated biological specimens or investigating in situ chemical reactions with high contrast and resolution. Moreover, our atomically thin graphene windows can also be applied more widely to other electron spectroscopy techniques, such as high-energy XPS, that require electron transparent windows for air operation.

■ ASSOCIATED CONTENT

Supporting Information

The Supporting Information is available free of charge on the ACS Publications website at DOI: 10.1021/acs.nanolett.6b03016.

Experimental details (PDF)

■ AUTHOR INFORMATION

Corresponding Authors

*E-mail: jp275@cornell.edu.
*E-mail: dm24@cornell.edu.

ORCID

Yimo Han: 0000-0003-0563-4611

Notes

The authors declare no competing financial interest.

■ ACKNOWLEDGMENTS

This work has been supported by the Cornell Center for Materials Research and NSF MRSEC (DMR-1120296). Yui Ogawa was partially supported by Grant-in-Aid for JAPS Fellows (No. 25-7288). We thank Megan Holtz, Pinshane Huang, Lola Brown, Cheol Joo Kim, Kibum Kang, Lujie Huang, Kan-Heng Lee, Mengnan Zhao, Jonathan Alden, Mark Marsslis, Yonghun Lee, John Grazul, Hao Shi, and Iwijn De Vlaminck for helpful discussions. We thank B-nano and Don Werder for help on airSEM.

■ REFERENCES

(1) Stokes, D. *Principles and Practice of Variable Pressure/Environmental Scanning Electron Microscopy (VP- ESEM)*; Wiley and Sons: West Sussex, 2008.
(2) Suga, M.; Nishiyama, H.; Konyuba, Y.; Iwamatsu, S.; Watanabe, Y.; Yoshiura, C.; Ueda, T.; Sato, C. *Ultramicroscopy* **2011**, *111*, 1650−1658.
(3) Nguyen, K.; Holtz, M.; Muller, D. *Microsc. Microanal.* **2013**, *19*, 428−429.
(4) Solomonov, I.; Talmi-Frank, D.; Milstein, Y.; Addadi, S.; Aloshin, A.; Sagi, I. *Sci. Rep.* **2014**, *4*, 1−7.
(5) Vidavsky, N.; Addadi, S.; Mahamid, J.; Shimoni, E.; Ben-Ezra, D.; Shpigel, M.; Weiner, S.; Addadi, L. *Proc. Natl. Acad. Sci. U. S. A.* **2014**, *111*, 39−44.
(6) Nguyen, K.; Holtz, M.; Richmond-Decker, J.; Muller, D. *Microsc. Microanal.* **2016**, *22*, 754−767.
(7) Lee, C.; Wei, X.; Kysar, J. W.; Hone, J. *Science* **2008**, *321*, 385−388.
(8) Bunch, J. S.; Verbridge, S. S.; Alden, J. S.; van der Zande, A. M.; Parpia, J. M.; Craighead, H. G.; McEuen, P. L. *Nano Lett.* **2008**, *8*, 2458−2462.
(9) Berry, V. *Carbon* **2013**, *62*, 1−10.
(10) Yuk, J. M.; Park, J.; Ercius, P.; Kim, K.; Hellebusch, D. J.; Crommie, M. F.; Lee, J. Y.; Zettl, A.; Alivisatos, A. P. *Science* **2012**, *336*, 61−64.
(11) Mohanty, N.; Fahrenholtz, M.; Nagaraja, A.; Boyle, D.; Berry, V. *Nano Lett.* **2011**, *11*, 1270−1275.
(12) Stoll, J. D.; Kolmakov, A. *Nanotechnology* **2012**, *23*, 505704−505709.
(13) Wojcik, M.; Hauser, M.; Li, W.; Moon, S.; Xu, K. *Nat. Commun.* **2015**, *6*, 7384.
(14) Kraus, J.; Reichelt, R.; Günther, S.; Gregoratti, L.; Amati, M.; Kiskinova, M.; Yulaev, A.; Vlassiouk, I.; Kolmakov, A. *Nanoscale* **2014**, *6*, 14394−14403.

DOI: 10.1021/acs.nanolett.6b03016
Nano Lett. 2016, 16, 7427−7432

(15) Li, X.; Cai, W.; An, J.; Kim, S.; Nah, J.; Yang, D.; Piner, R.; Velamakanni, A.; Jung, I.; Tutuc, E.; Banerjee, S. K.; Colombo, L.; Ruoff, R. S. *Science* **2009**, *324*, 1312−1314.
(16) Bae, S.; Kim, H.; Lee, Y.; Xu, X.; Park, J.-S.; Zheng, Y.; Balakrishnan, J.; Lei, T.; Kim, H. R.; Song; Il, Y.; Kim, Y.-J.; Kim, K. S.; Özyilmaz, B.; Ahn, J.-H.; Hong, B. H.; Iijima, S. *Nat. Nanotechnol.* **2010**, *5*, 574−578.
(17) Han, Y.; Nguyen, K.; Ogawa, Y.; Shi, H.; Park, J.; Muller, D. A. *Microsc. Microanal.* **2015**, *21*, 1111−1112.
(18) Joy, D. C. *J. Microsc.* **2002**, *208*, 24−34.

DOI: 10.1021/acs.nanolett.6b03016
Nano Lett. 2016, 16, 7427−7432